Supplemental Document

Optics Letters

Opto-electrical and polarization performance of a mesa-structured InGaAs PIN detector integrated with subwavelength aluminum gratings: supplement

JUNYANG ZHANG,[1,2,3] ZHENDONG GAO,[1,2,3] MIAO WANG,[4] GUOJIAN DING,[5] CHUNHUA DU,[1,3,6] YANG JIANG,[1,3] HAIQIANG JIA,[1,3,5] WENXIN WANG,[1,3,5] HONG CHEN,[1,3,5] AND ZHEN DENG[1,3,6,*]

[1] *Key Laboratory for Renewable Energy, Beijing Key Laboratory for New Energy Materials and Devices, Beijing National Laboratory for Condensed Matter Physics, Institute of Physics, Chinese Academy of Sciences, Beijing 100190, China*
[2] *University of Chinese Academy of Sciences, Beijing 100049, China*
[3] *Center of Materials and Optoelectronics Engineering, University of Academy of Sciences, Beijing 100049, China*
[4] *Suzhou Institute of Nano-Tech and Nano-Bionics (SINANO), Chinese Academy of Sciences, Suzhou 215123, China*
[5] *Songshan Lake Materials Laboratory, Dongguan, Guangdong 523808, China*
[6] *The Yangtze River Delta Physics Research Center, Liyang, Jiangsu 213000, China*
[*] *Corresponding author: zhen.deng@iphy.ac.cn*

Supplement DOI: https://doi.org/10.6084/m9.figshare.21453681

Parent Article DOI: https://doi.org/10.1364/OL.474555

Photo-electrical and polarization performance of mesa-structured InGaAs PIN detector integrated with subwavelength aluminum gratings: supplemental document

JUNYANG ZHANG,[1,2,3] ZHENDONG GAO,[1,2,3] MIAO WANG,[4] GUOJIAN DING,[5] CHUNHUA DU,[1,3,6] YANG JIANG,[1,3] HAIQIANG JIA,[1,3,5] WENXIN WANG,[1,3,5] HONG CHEN,[1,3,5] AND ZHEN DENG[1,3,6,*]

[1]Key Laboratory for Renewable Energy, Beijing Key Laboratory for New Energy Materials and Devices, Beijing National Laboratory for Condensed Matter Physics, Institute of Physics, Chinese Academy of Sciences, Beijing 100190, China
[2]University of Chinese Academy of Sciences, Beijing 100049, China
[3]Center of Materials and Optoelectronics Engineering, University of Academy of Sciences, Beijing 100049, China
[4]Suzhou Institute of Nano-Tech and Nano-Bionics (SINANO), Chinese Academy of Sciences, Suzhou 215123, China
[5]Songshan Lake Materials Laboratory, Dongguan, Guangdong 523808, China
[6]The Yangtze River Delta Physics Research Center, Liyang, Jiangsu 213000, China

FDTD Simulation: In order to optimize the grating parameters, finite-difference time-domain (FDTD) simulation was performed here. Figure S1 (a) was the diagram of the simulated model. Al was verified to be the most suitable metal for fabricated subwavelength gratings in short-wave infrared region, due to its large imaginary part of permittivity, low transmittance of TE wave, and good adhesion to the substrate in Refs [1, 2]. As seen in Ref [3], the operation wavelengths of the lattice-matched InP/InGaAs detectors located in 0.9-1.7 μm. In the communication field, 1310nm and 1550 nm were the mainstream used wavelength. Therefore, we fixed the incident wavelengths on 1310 nm and 1550 nm during the simulation process.

Figures S1 (b)-(i) showed the relationship between the polarization performance (transmittance of TM wave and TE wave, their extinction ratio (ER)) and the grating parameters (the height of SiO_2 (H), the height of the gratings (h), the period of the gratings (p) and the duty of the gratings (w/p)). As we can see from Figs. S1 (b) and (c), the TM/TE transmittance and ER varied periodically with H both under 1310 nm and 1550 nm. For TM transmittance and ER, the optimal ones didn't locate at the same H. Figures S1 (d) showed that the TM transmittance performed a decreasing trend when h increased. However, the TE transmittance decreased more rapidly, leading to the increase of ER; Conversely, the TM transmittance decreased with p increasing, while the TE transmittance increased in Fig. S1 (f), so the ER decreased accordingly. Figures. S(h) and S(i) illustrated the change rules between the transmittance, ER and w/p, respectively. When w/p was less than 0.9, the TE transmittance decreased more rapidly than the TM transmittance, and the ER increased. When w/p was greater than 0.9, the TE transmittance decreased slowly, and the ER began to decrease. According to effective medium theory [2], the ER will vanish at w/p=1 in theory. TM transmittance played an important role in detection and the polarization detection was sensitive to ER. In conclusion, to make a compromise between the transmittance and ER, the values of H, h, p and w/p were optimized to be 150 nm, 100 nm, 300 nm and 0.5, respectively in this paper. Figures S1(j) and (k), which illustrated the TM transmittance was above 0.4 and the ER was over 18dB in the whole spectrum, showed the performance of the TM/TE transmittance and ER at wavelengths ranging from 900 nm to 1700 nm with above chosen grating parameters.

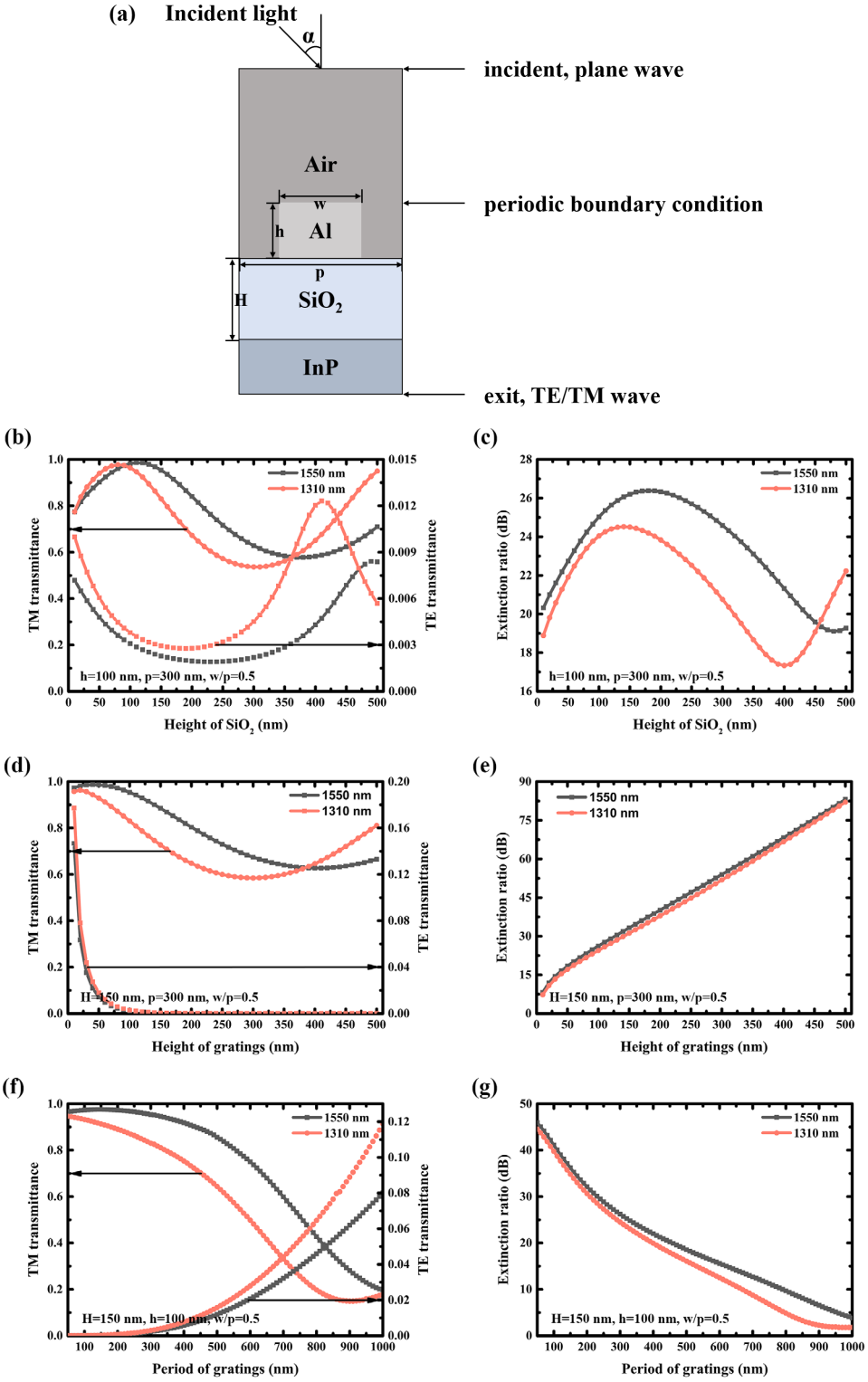
(a)
Incident light
α
incident, plane wave
Air
w
h
Al
periodic boundary condition
p
H
SiO2
InP
exit, TE/TM wave
(b)
1550 nm
1310 nm
TM transmittance
TE transmittance
h=100 nm, p=300 nm, w/p=0.5
Height of SiO2 (nm)
(c)
1550 nm
1310 nm
Extinction ratio (dB)
h=100 nm, p=300 nm, w/p=0.5
Height of SiO2 (nm)
(d)
1550 nm
1310 nm
TM transmittance
TE transmittance
H=150 nm, p=300 nm, w/p=0.5
Height of gratings (nm)
(e)
1550 nm
1310 nm
Extinction ratio (dB)
H=150 nm, p=300 nm, w/p=0.5
Height of gratings (nm)
(f)
1550 nm
1310 nm
TM transmittance
TE transmittance
H=150 nm, h=100 nm, w/p=0.5
Period of gratings (nm)
(g)
1550 nm
1310 nm
Extinction ratio (dB)
H=150 nm, h=100 nm, w/p=0.5
Period of gratings (nm)

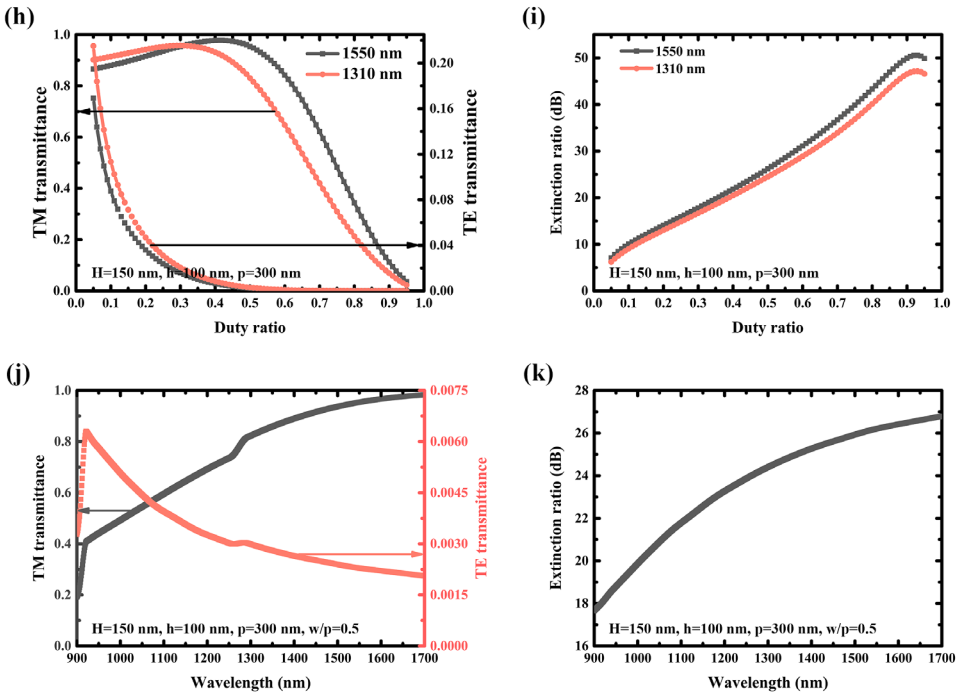

Fig. S1. (a) the diagram of the simulation model. (b) the relationship between the TM, TE transmittance and H; (c) the relationship between the ER and H; (d) the relationship between the TM, TE transmittance and h; (e) the relationship between the ER and h; (f) the relationship between the TM, TE transmittance and p; (g) the relationship between the ER and p; (h) the relationship between the TM, TE transmittance and w/p; (i) the relationship between the ER and w/p; (j) the TM and TE transmittance and (k) the ER while spectrum ranges from 900 nm to 1700 nm and H, h, p, w/p equals to 150nm, 100 nm, 300 nm, respectively.

Material Epitaxy: The cross-section diagram of the epitaxial structure grown by Metal-Organic Chemical Vapor Deposition (MOCVD) was shown in Fig. S2(a). First, a 500 nm heavily doped n^+ InP buffer layer was deposited on 2-inch n^+ InP substrate with the doping concentration of 2×10^{18} cm^{-3} to smooth the surface. Then, a 2 μm unintentional doped InGaAs light absorption layer was grown, followed by a 200 nm n- InP layer on the top. The p-region in our structure was achieved by zinc diffusion process by MOCVD. Finally, the traditional PIN structure could be seen in Fig. S2(b) and its band structure without bias was shown in Fig. S2(c) after diffusing.

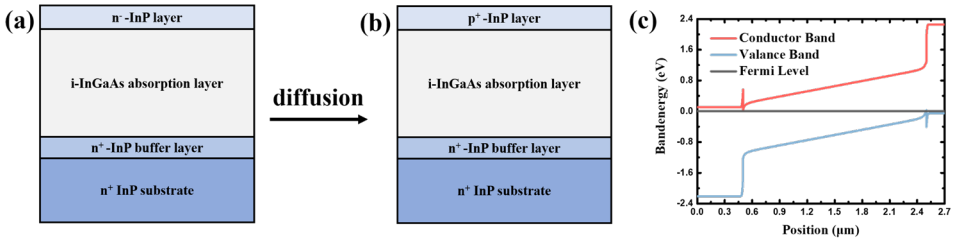

Fig. S2. The cross-section diagrams of (a) the epitaxial structure; (b) the structure after diffusing; (c) the band-structure without bias.

Fabrication Process: Figure S3 illustrated the fabrication process of our devices in this work. At the beginning, the mixed solution (H_3PO_4: H_2O_2: H_2O=2: 3: 30) and 37% hydrochloric acid solution were adopted to etch InP layer and InGaAs layer, respectively. The wet etching process stopped in n^+-InP buffer layer to make an isolation. Then, a 150 nm-thick SiN_x layer was grown to serve as passivation layer by inductively coupled plasma assisted plasma-enhanced chemical

vapor deposition (ICP-PECVD) technology. Whereafter, the SiN_x opening process was carried out by inductively coupled plasma (ICP) technology. Then, a 150 nm-thick SiO_2 dielectric layer was grown by ICP-PECVD and part of the SiO_2 was dry-etched for top p-electrodes opening by ICP. After that, Ti/Pt/Au alloy metals were deposited by electron beam evaporation (EBE) in two steps to form p-metal and p-metal pad. To expose a flat and new surface, the back of the devices was thinned mechanically for 10 μm. Subsequently, the n-electrode used Ni/Au/Ge/Ni/Au alloy metal in back by EBE and annealed 90 s at 390 ℃ in N_2 atmosphere to achieve ohmic contact. Finally, the fabrication of 300nm-spacing, 0.5-duty ratio (grating line-with/space), and 100nm-thick Al gratings along four angles was materialized with the help of the electron beam lithography (EBL) technology, followed by the Al EBE process, the lift-off process in 60℃ hot acetone and the 25s low-frequency ultrasonic process. Considering that the difference in grid resolution between the orthogonal and the diagonal orientation [4], the expose doses were different in 0°, 45° and 90° gratings, which were experimented to be 125 μC/cm^2, 135 μC/cm^2 and 115 μC/cm^2, respectively.

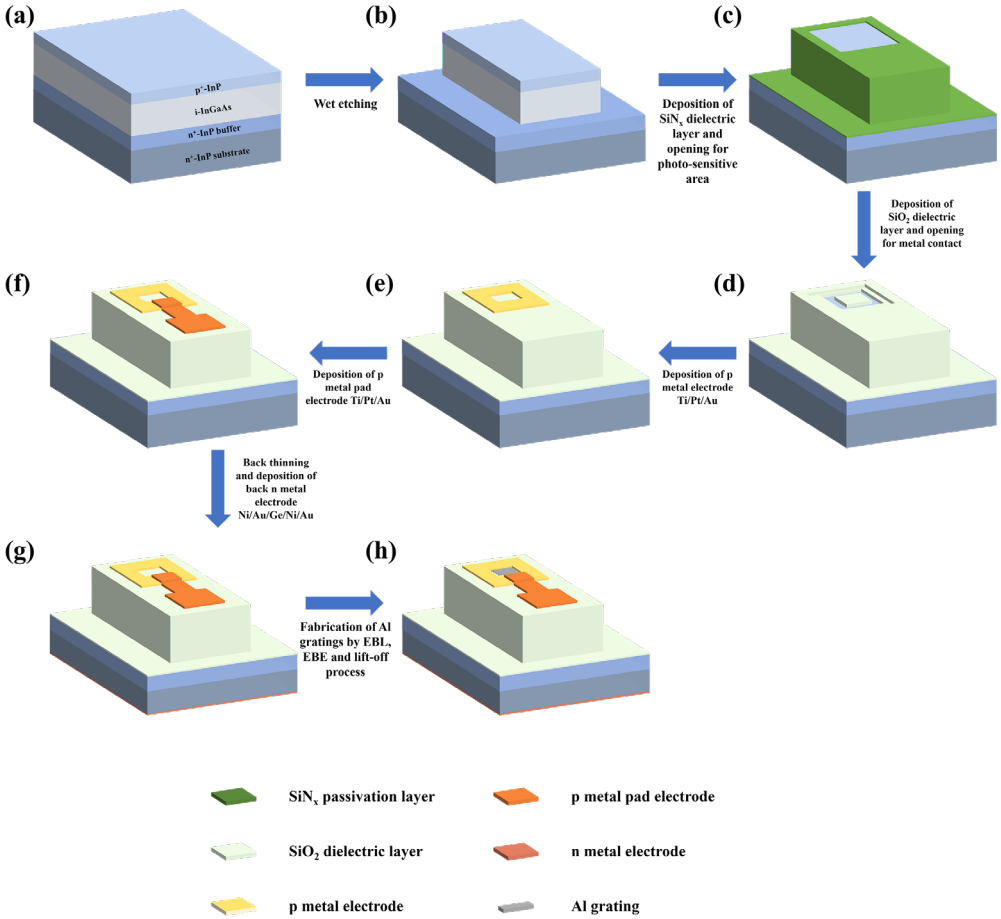

Fig. S3. The diagram of devices' fabrication process. (a) the epitaxial structure; (b) the wet etching process; (c) the SiN_x passivation layer deposition process and the photo-sensitive area opening process; (d) the SiO_2 dielectric layer deposition process and the p-metal opening process; (e) the top p and p pad electrodes deposition process; (f) the mechanical thinning process, the bottom n alloy electrode process and the electrodes annealing process; (h) the Al grating fabrication process.

Epilayer Characterization: High-resolution X-ray diffraction (HR-XRD) and atomic force microscope (AFM) were performed to verify the quality of the as-grown epilayer. Figure S4(a) showed (004) plane reflection of InGaAs layer obtained by ω/2θ scans along the growth

direction of InP/InGaAs PIN wafer. From the ω/2θ scan curve, the peaks of InGaAs epilayer and the InP substrate were almost coincide, and their full width at half maximum (FWHM) value was 40.99 arcsec. According to Bragg diffraction equation, the InGaAs epilayer was lattice matching with InP layer, which suggests that the In composition of InGaAs epilayer was 0.53. Figure S4(b) showed the AFM image with a 5 μm × 5 μm scanning area and the rms roughness is about 3.04 Å. The experimental results from HR-XRD and AFM indicated that a high-quality epi wafer was obtained and thus it was beneficial to fabricate high performance devices later.

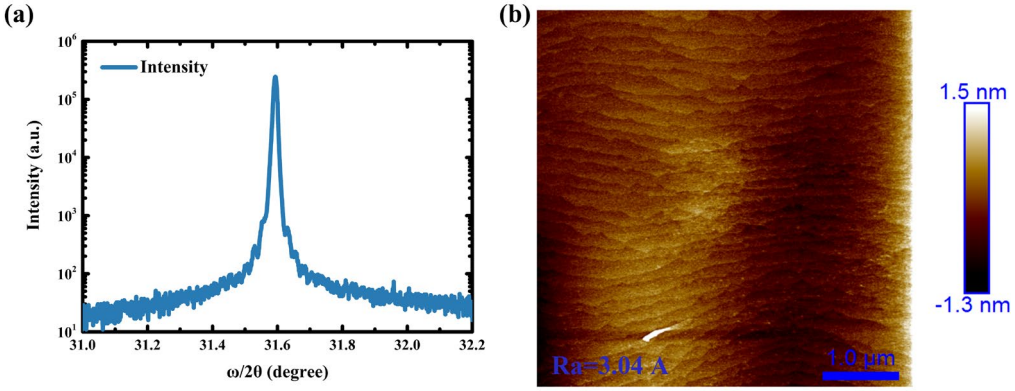

Fig. S4. (a) The HR-XRD ω/2θ scan of InP/InGaAs (004) plane and (b) the AFM image of a 5 μm × 5 μm scanning area for InP/InGaAs epi wafer.

Detectivity Calculation: The conventional definition of responsibility (R_i) and external quantum efficiency (η) is given by Ref [5],

$$R_i = \frac{I_{ph}}{P} \tag{S1}$$

$$\eta = \frac{hc}{q\lambda} \cdot \frac{I_{ph}}{P} = \frac{1240}{\lambda(\text{nm})} \cdot \frac{I_{ph}}{P} \tag{S2}$$

Where, h is the Plank constant; c in the speed of light in vacuum, equaling to 3×10^8 m/s; q is the electron charge, equaling to 1.6×10^{19} m/s; and λ is the wavelength in nm. Hence, the slopes of the inserts represent R_i, which equals to 0.79 A/W and 0.81 A/W for P1 and P0 at -0.1 V. The corresponding external quantum efficiencies (η) are 63.2% and 64.8%.

According to the Refs [6, 7], the Johnson noise limited detectivity D^* of the device is,

$$D^* = R_i \cdot \left[2qJ_d + \frac{4k_BT}{RA}\right]^{-1/2} \tag{S3}$$

Where, R_i is the responsibility; q is the electron charge, equaling to 1.6×10^{-19} C; J_d is the dark current density; k_B is the Boltzmann constant, equaling to 1.38×10^{-23} J/K; T is the operating temperature of devices; RA is the differential resistance, equaling to $\left(\frac{\partial J_D}{\partial V}\right)^{-1}$. The differential resistances R_0A at zero bias for P1 and P0 can be extracted from Fig. 3(a) in body text, which are 0.79×10^5 Ω·cm^2 and 0.92×10^5 Ω·cm^2, respectively. The corresponding D^* reaches 6.28×10^{11} cm·Hz$^{1/2}$/W and 6.88×10^{11} cm·Hz$^{1/2}$/W at 1550 nm and -0.1 V (room temperature), respectively.

Data Processing in Polarization Test: The specific definition of different regions is shown in Fig.S5 (device with 90 degree grating as an example). The grated region is circled by white dotted line, where subwavelength gratings locate. The un-grated region is the region circled between grey dotted line and white dotted line, surround by top electrode. The size of incident light beam is around 300 μm×300 μm, which is larger than grated region (95 μm×95 μm). Furthermore, metal can block the incident light and thus only grated region and un-grated region will play role in the light-induced carriers' generation.

Assuming that photo-generated carriers are generated uniformly, the actual signals induced by grated region $I_{0/45/90/135,\ actual}$ are formulated as following:

$$I_{0/45/90/135,\ actual}=I_{0/45/90/135,measure}-\frac{A_{un\text{-}grated\ region}}{A_{grated\ region}+A_{un\text{-}grated\ region}}I_{non,\ measure} \quad (S4)$$

Where, $I_{0/45/90/135,\ measure}$ and $I_{non,\ measure}$ represent the measured signals of devices with 0, 45, 90, 135-degree gratings and without grating.

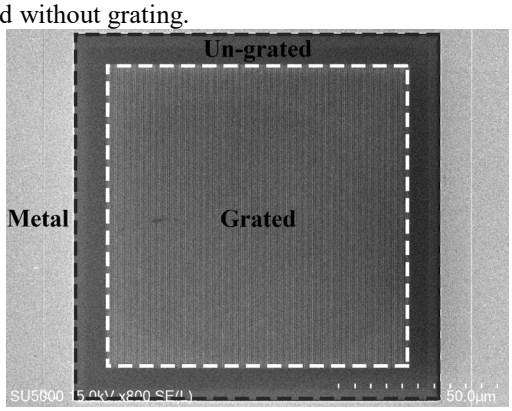

Fig. S5. The definition diagram of different regions.

Comparison Between Our Work and Other Reports: Table S1 gives the key parameters' comparison of detector integrated with subwavelength gratings between our work and other reports (experimental results).

Table S1. The Comparison of Detectors Integrated with Subwavelength Gratings Between Our Work and Other Reports (Experimental Results).

Structure	Material / Spectrum Response	D^* (cm • $Hz^{1/2}$/W)	Height of SiO_2 (nm)	Grating Material	Grating Parameters			Extinction Ratio	Ref
					Height (nm)	Period (nm)	Duty Ratio		
Mesa (single device)	InGaAs / 900-1700 nm	6.28×10^{11}	150	Al	100	300	0.5	≥ 18 : 1 @ 1550 nm	This Work
Planar (linear array)	InGaAs / 900-1700 nm	1.02×10^{12}	100	Al	100	300	0.5	≥ 23 : 1 @ 1550 nm	[8]
Planar (FPA)	InGaAs / 900-1700 nm	——	100	Al	100	400	0.5	≥ 22 : 1 @ 1550 nm	[9]
Planar (FPA)	InGaAs / 900-1700 nm	5.99×10^{11}	100	Al	100	300	0.5	≥ 8 : 1 @ 1550 nm	[10]
Planar (FPA)	Si / Visible	——	30	Al	70	140	0.5	58(±1.2) : 1 @ 625±5 nm	[11]
Planar (FPA)	InSb / MWIR	——	——	Ti/Au	10/150	400	0.5	50:1 (Best) @ 3.39 μm	[12]
Planar (single device)	Flexible plastic/ 400-800 nm	——	——	Al	70	278	0.5	≥ 1585 : 1 @ 400-800 nm	[13]
Planar (FPA)	InAs/GaSb SLs / 8-14 μm	4.56×10^{10}	——	Al	250	1000	0.5	50 : 1 @11.7 μm/ 80 K	[14]

References

1. Palik and D. Edward, in *Handbook of optical constants of solids* (1985).
2. S. Masui, S. Kadoya, M. Michihata, and S. Takahashi, Appl. Opt. **59**, 9469-9475 (2020).
3. J. Zhang, M. A. Itzler, H. Zbinden, and J.-W. Pan, Light: Sci. Appl. **4**, e286-e286 (2015).
4. B. Feng, Y. F. Chen, D. Sun, Z. Y. Yang, B. Yang, X. Li, and T. Li, Int. J. Extreme Manuf. **3**, 035201 (2021).
5. H. Lim, S. Tsao, W. Zhang, and M. Razeghi, Appl. Phys. Lett. **90**, 131112 (2007).
6. J. B. Rodriguez, E. Plis, G. Bishop, Y. D. Sharma, H. Kim, L. R. Dawson, and S. Krishna, Appl. Phys. Lett. **91**, 043514 (2007).
7. B. Chen, J. Yuan, and A. L. Holmes, Opt. Quant. Electron. **45**, 271-277 (2013).
8. D. Sun, Bo. F, Bo. Y, T. Li, X. M. Shao, X. Li, and Y. F. Chen, Opt. Lett. **45**, 1559-1562 (2020).
9. D. Sun, T. Li, Bo. Y, X. M. Shao, X. Li, and Y. F. Chen, Opt. Express **27**, 9447-9458 (2019).
10. C. Y. Sun, D. Sun, B. Yang, T. Li, X. M. Shao, X. Li and H. M. Gong, Infrared Phys. Technol. **123**, 104066 (2022).
11. V. Gruev, R. Perkins, and T. York, Opt. Express **18**, 19087-19094 (2010).
12. A. A. Cruz-Cabrera, S. A. Kemme, J. R. Wendt, R. R. Boye, T. R. Carter, and S. Samora, Proc. SPIE **6478**, 64780Q (2007).
13. L. Qin, J. T. Yang, C. G. Wang, C. Shen, Y. B. Wang, J. Tang and J. Liu, Opt. Commun. **434**, 118-123 (2019).
14. J. Zhou, Y. Zhou, Y. Shi, F. F. Wang, Z. C. Xu, Z. Z. Bai, M. Huang, L. L. Zheng, Z. M. Liang, Y. H. Zhu, Q. Q. Xu, Y. M. Shen, X. X. Ying, and J. X. Chen, Sci. China Inf. Sci. **65**, 122407 (2022).